Interface microstructure and composition of a $YBa_2Cu_3O_{7-x}$ / N / $YBa_2Cu_3O_{7-x}$ SNS edge junction with $CaRuO_3$ as the metallic barrier

S. Rozeveld*, K.L. Merkle and K. Char[a]

Materials Science Division and Science and Technology Center for Superconductivity, Argonne National Laboratory, Argonne, IL 60439.

[a]Conductus, Inc. 969 West Maude Avenue, Sunnyvale CA 94086.

* now at
Composite Materials and Structures Center, Research Complex - Eng A203, Michigan State University, E. Lansing, MI 48824

DTIC
ELECTE
JUN 1 6 1995
F

This document has been approved for public release and sale; its distribution is unlimited

Abstract:

Superconductor - normal - superconductor (SNS) edge junctions consisting of $YBa_2Cu_3O_7$ / $CaRuO_3$ / $YBa_2Cu_3O_7$ were fabricated on (001) $LaAlO_3$ substrates using laser deposition. These devices display an excess resistance which may be related to the SN interface and normal layer structure or composition. High-resolution and conventional transmission electron microscopy were employed to investigate the SN interface structure to determine the degree of interface matching and possible interfacial defects. Energy-loss spectroscopy and energy dispersive x-ray analysis were performed on the $CaRuO_3$ film and near interface regions to determine the normal layer composition and to quantify the extent of interdiffusion between the $CaRuO_3$ and YBCO films. Results are compared to recent investigations of SNS edge junctions consisting of $YBa_2Cu_3O_{7-x}$ / $YBa_2Cu_{2.79}Co_{0.21}O_{7-x}$ / $YBa_2Cu_3O_{7-x}$.

1. Introduction

Considerable effort has been devoted to development of superconducting - normal - superconducting (SNS) Josephson junctions in both trilayer and edge designs using $YBa_2Cu_3O_{7-x}$ (YBCO) thin films and various normal materials. Barrier materials include the noble metals Au[1], Ag[2, 3] and Ag-Au alloys[2][4]. Metallic oxide barrier layers have also been investigated such as $PrBa_2Cu_3O_7$[5-8], $Y_{0.6}Pr_{0.4}Ba_2Cu_3O_7$[9], normal-YBCO[10], $SrTi_xNb_{1-x}O_3$[11] and $La_{0.5}Sr_{0.5}CoO_3$, Ca-doped YBCO, Co-doped YBCO, $CaRuO_3$, $SrRuO_3$,, $Sr_{0.5}Ca_{0.5}RuO_3$ and $La_{1.4}Sr_{0.6}CuO_4$[12-14].

Recent investigations have shown that an excess resistance was present in SNS junctions for the following normal layers Ag[2], Au[4], $CaRuO_3$, $SrRuO_3$, and $La_{0.5}Sr_{0.5}CoO_3$ [12-14]. Typically, the R_nA products (R_n = normal state resistance, A = junction area) varied from 10^{-7} to 10^{-8} Ωcm^2 which was 10 to 100 times higher than expected[13, 14]. The origin of the excess resistance may be due to several sources

19950613 000

including mismatch in carrier density, thermal expansion, or lattice constant[13]. It has been proposed that the excess resistance is due to the lattice mismatch between $CaRuO_3$ and YBCO which produces oxygen depleted or disordered regions near the interface[13].

In this paper we discuss the results of transmission electron microscope (TEM) investigations of SNS edge junctions with $CaRuO_3$ as the metallic barrier. $CaRuO_3$ was selected as a viable barrier material since the normal state conductivity was suitable for device applications and the thermal expansion and lattice constant are well matched to YBCO[12]. Only a few studies so far have investigated the interface microstructure of SNS junctions in detail[15]. In view of the need for further study, our investigations have focused on determining the structure of the YBCO / $CaRuO_3$ interface at the atomic scale and measuring the composition of the normal layer and the extent of interdiffusion between the S and N layers[13]. This study was also undertaken to compare the interface microstructure of the $CaRuO_3$ junctions to recent studies of $YBa_2Cu_3O_{7-x}$ / $YBa_2Cu_{2.79}Co_{0.21}O_{7-x}$ / $YBa_2Cu_3O_{7-x}$ SNS junctions[16]. The latter junctions do not display an excess resistance; thus, comparing interface features and/or defects in these junctions may provide additional insight into the origin of the excess resistance observed in the $CaRuO_3$ junctions.

2. Experimental

Cross sectional TEM foils were prepared by mechanical dimpling and polishing followed by ion-beam thinning to perforation. Ion-thinning was performed in a Gatan ion-mill at 4kV at an incident angle of 18°, the accelerating voltage and angle were reduced to 3 kV and 14° for the last 1-2 hours of preparation. All ion-beam thinning was performed with a liquid nitrogen cooled specimen holder to reduce oxygen loss and defect formation. All TEM foils were prepared from a single 10 mm^2 sample to minimize variations in deposition conditions.

TEM experiments were performed on a JEOL 4000 EXII microscope at an accelerating voltage of 200 keV. An objective aperture of radius 2.0 nm^{-1} was used and the other microscope parameters were as follows: spherical aberration coefficient, Cs, was determined to equal 1.3 mm (at 200 kV), semi-angle of convergence was 2 mrad., the Gaussian spread of focus was 9 nm. High-resolution simulations were calculated using the EMS suite of programs [17]. The unit cells of $CaRuO_3$ and YBCO were divided into 3 slices along the [110] beam direction; therefore, the thickness of each slice did not exceed 0.2 nm. Multislice calculations were conducted using 128 x 64 and 64 x 64 sampling sizes for YBCO and $CaRuO_3$, respectively. Absorption was not included in the image simulations. The structure of $CaRuO_3$ was assumed to be cubic perovskite for the

A-1

purposes of this study, although simulations were also conducted for the orthorhombic unit cell of CaRuO3 presented in Fig. 2. The lattice parameters of $CaRuO_3$ were taken from the work of Van Loan[18], Debye-Waller temperature coefficients were assumed to equal 0.005 nm^2 for Ca, Ru and O. The lattice parameter values and Debye-Waller coefficients of YBCO were taken from the work by Jorgensen *et al.*[19] assuming a composition of $YBa_2Cu_3O_{6.93}$ for the superconducting film.

Analytical electron microscopy experiments were conducted on a 200 keV cold field emission TEM (Hitachi HF-2000) equipped with a Gatan 666 parallel electron energy-loss (EELS) Spectrometer and a Link System ultra thin window (UTW) X-ray detector for X-ray chemical analysis. The probe size for all experiments was ~2 nm. A cold stage specimen holder was used to lower the specimen temperature to -180°C to minimize sample contamination.

Selected area diffraction patterns of YBCO, $CaRuO_3$, $CaTiO_3$ films and $LaAlO_3$. substrate were recorded and measurements were made of several lattice plane spacings to determine the lattice parameters. The measurement error was less than ±0.005 nm. The films were deposited onto $LaAlO_3$ which has a Rhombohedral perovskite structure with hexagonal lattice parameters of **a** = **b** = 0.5364 nm and **c** = 1.311 nm, $\alpha = \beta = 90°$, $\gamma = 120°$ [20]. However, $LaAlO_3$ is often described as pseudo-cubic perovskite with **a** = 0.3790 nm assuming the following orientation relationship:

$(012)_{hex} \parallel (001)_{cubic}$ and $[110]_{hex} \parallel [1\bar{1}0]_{cubic}$.

Measurements of the lattice parameters of the films were made relative to the $LaAlO_3$ substrate.

3. Results and Discussion

A schematic of an edge junction investigated in this work is shown in Fig. 1. Films of YBCO, $CaTiO_3$, and $SrTiO_3$ were deposited sequentially onto a $LaAlO_3$ substrate using an off-axis laser ablation technique; details of the fabrication steps of the edge junctions are discussed elsewhere [12]. After the films were deposited, the edge was patterned by *ex-situ* Ar ion-beam milling and standard photolithography techniques. The $CaRuO_3$ layer was then deposited at 700°C followed by the second YBCO film at 780°C. The nominal thicknesses of the $CaRuO_3$ layer in this study was 20 nm, whereas the YBCO films were approximately 200 nm thick.

Barrier materials were selected based on several criteria. The conductivity of the barrier layer should have metallic behavior and should not be sensitive to oxygen stoichiometry or doping. In addition, the thermal expansion and lattice parameter should

be well matched to YBCO [12]. Several materials met these requirements but initial measurements of SNS junctions favored $CaRuO_3$ due to its desirable R_n properties. $CaRuO_3$ has an orthorhombic perovskite structure with lattice parameters **a** = 0.554 nm, **b** = 0.536 nm and **c** = 0.768 nm[18, 21]. The unit cell of a simple orthorhombic perovskite is shown in Fig. 2 along with the pseudo-cubic unit cell; the structure of similar orthorhombic perovskite compounds are discussed elsewhere[22-27]. Callaghan *et al.* [26] have measured the conductivity of several ruthenium oxides ($CaRuO_3$, $SrRuO_3$, $BaRuO_3$, $Ba_{5/6}Sr_{1/6}RuO_3$, Sr_2RuO_4, $BaRu_{2/3}Mg_{1/3}O_3$). Of these oxides, only $BaRu_{2/3}Mg_{1/3}O_3$ had poor conductivity which was attributed to its complex ordered hexagonal structure with a large Ru-Ru separation. For the purposes of this work, we will refer to $CaRuO_3$ as pseudo-cubic since this is consistent with previous work. The lattice parameter of $CaRuO_3$ is 0.385 nm assuming a pseudo-cubic structure and is well matched to the YBCO film (**a** = 0.382 nm, **b** = 0.387). Thus, the $CaRuO_3$ film is expected to grow epitaxial onto YBCO with the following orientation relationship:

$$(001)_{CaRuO3} \parallel (001)_{YBCO} : [110]_{CaRuO3} \parallel [110]_{YBCO}.$$

The orientation relationship between $CaRuO_3$ and YBCO is presented schematically in Fig. 3. The junctions were patterned parallel to a [110] direction, thus conveniently allowing crosssection TEM observations of the junction structure along [110].

A TEM micrograph of an edge junction viewed in cross-section is shown in Fig. 4 near the [110] zone axis. The $LaAlO_3$ substrate and YBCO and $SrTiO_3$ films are readily distinguishable owing to the differences in atomic number. The uniformity of the upper YBCO and $SrTiO_3$ films in Fig. 4 is interrupted periodically. This is due to the nucleation of small particles in the lower YBCO film which were identified as **a**-axis YBCO. Previous studies have shown that the **a**-axis particles also introduce porosity into the $SrTiO_3$ film[15].The particles shown in Fig. 4 appear to originate within the first YBCO film; however, there is evidence that **a**-axis particles also can nucleate at the YBCO / $LaAlO_3$ interface[28].

The active interface region of the junction presented in Fig. 4 is shown in greater detail in Fig. 5 . The YBCO | $CaRuO_3$ | YBCO interfaces are clearly stepped and the $CaRuO_3$ film gradually approaches the $LaAlO_3$ substrate. The interface steps vary in height ranging between 2 and 6 nm and have an irregular longitudinal spacing of ~80 nm. The $CaRuO_3$ film in this sample was 10 nm thick on average and quite uniform except at the interface steps; at these regions the thickness of the barrier layer was approximately 20 nm. One expects that the interface morphology (i.e. step size and distribution) is a function of the ion-beam milling parameters and annealing conditions prior to deposition

of the $CaRuO_3$ film (at 700°C). In addition, the *ex situ* Ar ion-beam milling is expected to damage the YBCO film. This ion beam induced damage may also affect the junction properties; thus, determining the extent of recovery of the YBCO film is important. However previous measurements by Char *et al.* [13] on YBCO / YBCO junctions that were fabricated by an identical procedure, but with no barrier layer showed that J_c properties of the YBCO film did not degrade. This indicates that the ion-damaged YBCO should be able to recover completely during the anneal.

Moiré fringes were often observed near the steps adjacent to the top interface of the $CaRuO_3$ layer as shown in Fig. 5 . The fringe spacing was approximately 3.5 nm measured parallel to $[\bar{1}10]_{CaRuO3}$ and were located near the upper SN interface. This observation raises an important question concerning the nature of the YBCO | CaRuO3 interface. Since the lattice parameters of $CaRuO_3$ and YBCO are nearly equal, a moiré fringe will not be introduced from overlapping YBCO and $CaRuO_3$ films unless the films are either rotated from the expected orientation relationship or there is a significant difference in the lattice parameters. Of course, the presence of another phase could also account for the observed moiré fringes. Olsson and Char[15] studied similar SNS junctions prepared by a slightly different processing method and observed Y_2O_3 particles at the $CaRuO_3$ |YBCO interface. However, while Y_2O_3 particles were also observed in the present study, the particles were associated with porosity in the YBCO films and were not observed near the interface. Thus, the moiré fringes are due to another source; this is discussed in more detail later.

The $CaTiO_3$ buffer layer (with a pseudo-cubic lattice parameter of a=0.382 nm) which is also visible in Fig. 5 forms epitaxial onto the LaAlO3 substrate (a=0.397 nm) with the orientation relation $(001)_{CaTiO3} \parallel (001)_{YBCO}$: $[110]_{CaTiO3} \parallel [110]_{YBCO}$. Nevertheless, unusual fringe spacings and the corresponding periodicities in selected area electron diffaction (SAD) patterns, are seen in some areas, such as indicated in Fig. 5. This suggests that the buffer layer contains a complex defect structure and possibly a different phase in some regions.

The active interface region of another junction is shown in Fig. 6 near the [110] zone axis. The TEM image presented in Fig. 6 shows that the position of the $CaRuO_3$ layer varies and does not follow a constant slope relative to the substrate. This behavior is typical of the junctions observed, i.e., the slope will vary over sections of the same $CaRuO_3$ layer. These variations may be attributed to nonuniform ion-beam etching of the first YBCO film during fabrication. The boxed region of the interface is shown in greater detail in Fig 7; the (001) and $(\bar{1}10)$ lattice planes are visible in both the YBCO and

$CaRuO_3$ films (the lattice spacings are 0.38 nm and 0.27 nm for the (001) and $(\bar{1}10)$ lattice planes, respectively). The $CaRuO_3$ and YBCO are well matched across the interface, hence no misfit dislocations were observed along the broad faces on the interface.

The $CaRuO_3$ film is epitaxial with respect to the YBCO films at both the broad faces of the interface and the steps and no amorphous phases or Y_2O_3 precipitates were observed at the interfaces. Nevertheless, in Fig. 7 a small segment of the $CaRuO_3$ film shown appears rotated ~3° with respect to the lower portion of the $CaRuO_3$ layer. The origin of this defected $CaRuO_3$ region is not known, but may also involve the modification of the structure due to interdiffusion. The latter is expected to be enhanced along the a,b planes of YBCO. Thus, the location of the modified $CaRuO_3$ regions at the steps is consistent with such an explanation. Overlapping films of YBCO and $CaRuO_3$ with a rotation of the observed magnitude would produce moiré fringes with a 0.7 nm spacing along $[\bar{1}10]$, assuming the interfering reflections are $(003)_{YBCO}$ and $(001)_{CaRuO3}$. Such small defective regions of $CaRuO_3$ are quite common and explain the frequent observation of moiré fringes at SNS junction steps. It should also be noted that the rotation is accompanied by a lattice distortion as indicated by the parallelogram in Fig. 7.

Image simulations were conducted to interpret the contrast observed in the HRTEM images shown in Fig. 7. A best fit for the images was obtained using a thickness value of 11 nm and defocus of -90 nm for both YBCO and $CaRuO_3$. Using these parameters in the simulations yielded a white atom contrast for the Cu positions in YBCO as shown by the model overlain on the simulations in Fig. 8. The white contrast in the $CaRuO_3$ was located between the Ca atoms.

One important observation from Fig. 7 is that the $(\bar{1}10)$ planes of YBCO and $CaRuO_3$ are well matched across the broad sections of the interface. Thus, the orientation relationship between the YBCO and $CaRuO_3$ is given by:

$$(001)_{YBCO} \parallel (001)_{CaRuO3} : [110]_{YBCO} \parallel [110]_{CaRuO3}.$$

The matching of the $(\bar{1}10)$ lattice plane across the interface can be described by the model overlain on the simulations shown in Fig. 8. Here, the unit cells are displaced by 1/2[010] as depicted earlier in Fig. 3 so that the Ru atoms are nearest neighbors to O(1) of YBCO and maintain an octahedral coordination. However, it is important to note that determination of the terminating plane of either YBCO or $CaRuO_3$ was not possible from Fig. 7. Thus, other configurations are possible and further work is needed to verify the atomic-scale interface structure.

Another SNS junction is shown in cross section in Fig. 9 near the [110] zone axis with the interface region shown in greater detail in Fig. 10. As before, the SN interface is clearly stepped and the $CaRuO_3$ layer eventually merges with the $LaAlO_3$ substrate over a distance of several microns. One interesting feature is that the $CaRuO_3$ layer shown in Fig. 10 appears to consist of a double layer, i.e., two films separated by regions of darker contrast. This type of film growth was observed in several different junctions and has not been reported previously. Since the area shown was too thick for HREM imaging, lattice spacings are not visible in Fig. 10; however, selected area diffraction patterns of the interface region were recorded and a representative pattern is shown in Fig. 11. Lattice planes corresponding to $CaRuO_3$ reflections were measured and the data are presented in Table 1 along with possible (hkl) indices of cubic $CaRuO_3$ planes.

Table 1

Reflection	Measured lattice spacing	Possible (*hkl*) indices (cubic)	Calculated lattice spacing
1	0.159 nm	$(1\bar{1}2)$	0.157 nm
2	0.116 nm	(113)	0.116 nm
3	0.172 nm	(021)	0.172 nm

Assuming $CaRuO_3$ is cubic perovskite with a lattice parameter of 0.385 nm, the measured lattice plane spacings and angles in Fig. 11 correspond well to calculated values for the $(1\bar{1}2)$, (113), and (021) planes; thus, the zone axis in portions of the $CaRuO_3$ film shown in Figs. 9 and 10 is $[51\ \bar{2}]$ rather than [110] .

A possible explanation for the "double" $CaRuO_3$ layer and the reflections in Fig. 11 is that another phase has formed at the interface due to interdiffusion between the $CaRuO_3$ and YBCO layers or that a non-stoichiometric $CaRuO_3$ layer was initially deposited locally. Using energy dispersive x-ray spectroscopy (EDS) and electron energy-loss spectroscopy (EELS) and energy dispersive X-ray analyses we have recently shown that considerable interdiffusion does occur between the YBCO and $CaRuO_3$ films. A representative EDS spectrum of the $CaRuO_3$ film is shown in Fig. 12. As expected, the film consists mainly of Ca, Ru, and O; however, measurable amounts of Ba, Cu, and Y were also observed. Because the EDS technique has limited spatial resolution, EELS spectra were also recorded from the CaRuO3 and YBCO films at several distances from the interface. Typical spectra are presented in Figs. 13a and 13b. In Fig. 13b, the background was fitted and removed to show the relevant edges. The relative amounts of Ba and O were quantified, using the approach employed in previous studies[29, 30]. One

important result from the EELS studies is that the Ba / O ratio in the $CaRuO_3$ film is ~0.10, which was much higher than expected. If we assume that Ba substitutes only for Ca, then the normal film composition would be $Ba_{0.3}Ca_{0.7}RuO_3$. The relative amounts of Ca and Ru in the YBCO and Cu and Y in the $CaRuO_3$ film were not quantified. The EELS studies indicate that the effective penetration depth of Ca into YBCO is approximately 10 nm. Similar diffusion depths of Ba into $CaRuO_3$ have also been measured[31].

It is interesting to note that the thickness of the $CaRuO_3$ film shown in Fig. 10 is ~25 nm and appears to consist of three layers, each ~8 nm in thickness. This thickness correlates with the EELS data concerning the diffusion depth of Ba into $CaRuO_3$. Therefore, one explanation for the "double" $CaRuO_3$ layer is that Ba has diffused ~8 nm into the $CaRuO_3$ film from both interfaces. Thus it is possible that only the regions of the $CaRuO_3$ film showing bright contrast in Fig. 10 have the [51 $\bar{2}$] orientation indicated by Fig. 11.

4. Summary and Conclusions

TEM investigations were conducted on SNS junctions with $CaRuO_3$ as the normal layer. The TEM investigations show that the SN interface was stepped and gradually approached the substrate over a distance of several microns. The step heights and spacings between steps varied considerably, probably due to variations in local ion-beam milling rates. The thickness of the $CaRuO_3$ film was fairly uniform over the broad faces of the interface; however, the $CaRuO_3$ film was usually two times thicker at the interface steps. The $CaRuO_3$ was found to grow epitaxially onto YBCO and the SN interfaces were free of amorphous phases. In contrast to previous reports, no precipitates of Y_2O_3 were observed in the present samples at SNS interfaces. The orientation relationship between the $CaRuO_3$ and YBCO was given by:

$$(001)_{YBCO} \parallel (001)_{CaRuO3} : [110]_{YBCO} \parallel [110]_{CaRuO3}.$$

Small portions of the $CaRuO_3$ film showed a distorted lattice and deviated from the above orientation with YBCO. Such deviations are thought to produce the moiré fringes which are frequently observed near the SN interface steps due to overlapping YBCO and $CaRuO_3$ films. Although interdiffusion is a likely cause, another possible explanation of this behavior is that the misorientation is induced by thermal stress due to the poor match in thermal expansion properties between $CaRuO_3$ and YBCO at the interface steps (the mismatch in thermal expansion coefficients between the YBCO and $CaRuO_3$ films is larger at the steps by a factor of two compared to the broad faces of the interface due to the anisotropic properties of YBCO).

Other sections of the $CaRuO_3$ film showed, as in Figs. 9 and 10 unusual bright / dark / bright contrast in which the film appeared to be divided into three layers; each layer was ~8 nm thick. The layered contrast was observed in several different junctions, but not over the entire $CaRuO_3$ film. The total thickness $CaRuO_3$ in these segments was ~25 nm. Diffraction patterns indicated that the orientation of this portion of the $CaRuO_3$ film was $[51\bar{2}]$ rather than [110]. It is thought that only the outer regions of the CaRuO3 film (i.e., those portions showing bright contrast in Fig. 10) have the $[51\bar{2}]$ orientation. However, this has yet to be verified.

The unusual contrast of the interlayer in Fig. 10 may also be due to the formation of a second phase at the interface. However, EDS experiments indicate that the film composition is mainly Ca, Ru, and O as expected and the levels of Ba, Cu, and Y in the $CaRuO_3$ layer do not exceed ~10%. The electron energy loss data indicate that the Ba / O ratio in the $CaRuO_3$ film is ~0.10, which was higher than expected. Assuming that Ba substitutes only for Ca in the normal layer, the normal film composition would be $Ba_{0.3}Ca_{0.7}RuO_3$. Unfortunately, very little is known about the phase diagrams in these complex oxides.

Electron energy-loss experiments also show that interdiffusion of Ba and Ca occurs between the $CaRuO_3$ and the YBCO films over a depth on the order of ~10nm from the SN interfaces. Since this distance is comparable to the thickness of the layered contrast of the $CaRuO_3$ film shown in Fig. 10, it is tempting to conclude that structural changes due to interdiffusion is the origin of the contrast; that is, the layered contrast is a result of orientation and compositional changes within ~8 nm of the SN interfaces. On the other hand, however, if interdiffusion is the cause of these changes one would expect to observe this behavior over the entire $CaRuO_3$ layer.

To what degree the microstructural features and composition changes in the normal layer affect the junction properties remains the central question. The TEM observations have shown that there are considerable variations in the local defect structures of the junctions and their uniformity is far from ideal. This undoubtedly impacts considerably on the large fluctuations in junction transport property values that have been observed in the past. On the other side, most of the junctions are quite well structured at the atomic scale. In particular no gross defects, such as amorphous phases were found at the SNS interfaces.

One would expect that isolated defects, although they may significantly alter the local transport properties, would not significantly affect the overall resistance of a junction, since the latter would be dominated by the majority properties of the interfacial connections. In relating TEM observations of the interfacial structure and composition one should also consider that only a minute fraction of the interfacial area associated with a typical SNS junction is being sampled.

The unavoidable interfacial stresses between $CaRuO_3$ and YBCO may introduce oxygen depleted regions near the interface as has been proposed earlier[9], although no significant structural changes of the YBCO were found in the near interface regions in the present study. Further studies are necessary to evaluate the local oxygen stoichiometry in the vicinity of the interfaces. The compositional changes in the cation population observed in this study may also be important. However, T_c and J_c properties of similar SNS junctions were not adversely affected by Ca diffusion and subsequent Ba depletion in the YBCO near the interface[12-14]. Unfortunately very little is known about the detailed transport properties of mixed ruthenates, including their anisotropy and their dependence on impurity additions [26].

Since the YBCO/$CaRuO_3$ interfaces are on average quite well structured, with the exception of some sections that may include second phases or unusual epitaxial relations, we conclude that the excess interfacial resistance observed in $CaRuO_3$ junctions must be attributed to changes in chemical composition due to either oxygen deficiency and/or cation interdiffusion in a region on the order of 10 nm in the vicinity of the interfaces.

Recent investigations of SNS edge junctions consisting of $YBa_2Cu_3O_{7-x}$ / $YBa_2Cu_{2.79}Co_{0.21}O_{7-x}$ / $YBa_2Cu_3O_{7-x}$ have shown that no amorphous phases or precipitates are present at the interface and that Cu-O planes are continuous across the normal layer. In general, the $YBa_2Cu_3O_{7-x}$ / $YBa_2Cu_{2.79}Co_{0.21}O_{7-x}$ / $YBa_2Cu_3O_{7-x}$ (Co-doped) junctions have fewer structural imperfections than the $CaRuO_3$ junctions. Moreover, the much more gradual chemical composition changes expected may explain the absence of an excess resistance in the Co-doped junctions. These observations lend strength to the argument that the excess resistance is related to the compositional changes at the interfaces between $CaRuO_3$ and YBCO films.

Acknowledgements

*This work was supported by the National Science Foundation (DMR 91-20000) through the Science and Technology Center for Superconductivity (SR), and the U.S. Department of Energy, Basic Energy Sciences-Materials Science under Contract No. W-31-109-ENG-38 (KLM). The use of the JEOL 4000EXII at the Electron Microscopy Center

of Argonne National Laboratory and the Hitachi HF2000 at Northwestern University through the STCS is acknowledged.

Figure captions

Fig. 1. Schematic of the SNS edge junction geometry in cross-section.

Fig. 2. Schematic of an orthorhombic and pseudo-cubic perovskite $CaRuO_3$ structure and the orientation relationship. The lattice parameters of the orthorhombic structure are **a** = 0.554 nm, **b** = 0.536 nm, **c** = 0.768 nm. For the pseudo cubic structure, the lattice parameters are **a'** = **b'** = 0.385 nm, **c'** = 0.384 nm, $\alpha = \beta = 90°$, $\gamma = 88°$.

Fig. 3. Models of the YBCO and $CaRuO_3$ unit cells in [100] and [110] normal views. The unit cells are displaced by 1/2[010] to show one possible configuration for lattice matching across the interface.

Fig. 4. Transmission electron microscopy image of a typical SNS edge junction near the [110] zone axis. The interface region denoted by the box is shown in greater detail in Fig. 5. Periodic disruptions in the uniformity of the upper YBCO and $SrTiO_3$ films are due to the presence of a-axis YBCO particles.

Fig. 5. Transmission electron microscopy image of the active interface region of a SNS edge junction near the [110] zone axis. The SN interfaces are stepped and gradually approach the $LaAlO_3$ substrate. The thickness of the $CaRuO_3$ layer was nominally 10 nm along the broad faces of the interface and approximately 20 nm at the steps. The $CaTiO_3$ layer was approximately 30 nm thick and contains planar defects on (111) planes. The fine spacing in the $CaTiO_3$ layer corresponds to 0.73 nm ($3 \times \mathbf{d}_{(111)CaTiO3}$) and the larger spacing corresponds to 2.9 nm ($12 \times \mathbf{d}_{(111)CaTiO3}$).

Fig. 6. Transmission electron microscopy (TEM) image of the SN interface of an edge junction near the [110] zone axis. The interface region within the box is shown in Fig. 7 Note the defects in the $CaTiO_3$ layer and the non-uniform film thickness for the $CaTiO_3$ and $CaRuO_3$ films. Moiré fringes are visible in areas of the $CaRuO_3$ film.

Fig. 7. High resolution transmission electron microscopy image showing the detail in the interface on the junction presented in Fig. 6. The $CaRuO_3$ film is epitaxial with respect to the YBCO over the broad faces and steps in the interface and the lattices are well structured up to the interface, i.e., no amorphous phases or precipitates were observed. A segment of the $CaRuO_3$ film is rotated

approximately 3° with respect to the lower $CaRuO_3$ film about the [110] zone axis.

Fig. 8. Simulation of the high resolution TEM image shown in Fig. 7. The simulation corresponds to the region nearest the edge of the foil. A best fit for the images was obtained using a thickness value of 11 nm and defocus of -90 nm for both YBCO and $CaRuO_3$. The thickness and defocus values varied slightly across the sample; at the thicker regions a best fit was found using a thickness of 13 nm and a defocus of -70 nm. Simulations yielded a white atom contrast near the Cu positions in YBCO as shown by the model overlain in Fig. 8. The white contrast in the $CaRuO_3$ was located between the Ca atoms. Since the terminating plane of YBCO or $CaRuO_3$ could not be determined from Fig. 7, several configurations are possible to describe the atomic coordination across the interface. Thus, the unit cells of YBCO and $CaRuO_3$ drawn in the simulations should be viewed only as an aid to the reader.

Fig. 9. Transmission electron microscopy image of the SN interface of a edge junction near the [110] zone axis. Small clusters in the $LaAlO_3$ substrate are due to beam damage in the TEM. The interface region denoted by the box is shown in greater detail in Fig. 10.

Fig. 10. Transmission electron microscopy image of the SN interface region of the junction shown in Fig. 9. The CaRuO3 layer appears to consist of a double layer, i.e., two films separated by pockets of darker contrast. Moiré fringes are present in some areas of the CaRuO3 film. Planar defects are present on the $(1\ \bar{1}\ 1)$ plane of the $CaTiO_3$ film.

Fig. 11. Selected area diffraction pattern of the interface region shown in Fig. 10. CaRuO3 reflections are labeled as $(1\ \bar{1}2)$, (113) and (021). Note the intensity at $1/2\{113\}_{\text{cubic-CRO}}$ positions; these reflections are kinematically forbidden for an ideal cubic perovskite structure. For clarity, the following abbreviations were used: LAO = $LaAlO_3$ and CRO = $CaRuO_3$.

Fig. 12. Energy dispersive x-ray spectra recorded from the $CaRuO_3$ film. Small amounts of Ba, Cu, and Y were present in the normal layer.

Fig. 13. (a) Electron energy loss spectra recorded from the $CaRuO_3$ film and YBCO films near the interface. The spectrum labeled CaRuO3 was recorded with the electron beam at the center of the CaRuO3 film. The probe size was ~2 nm. The

The spectra labeled YBCO1 and YBCO2 were recorded in the YBCO at a distance of 5 nm and 10 nm, respectively, from the SN interface.

(b) Energy loss spectra shown in (a) after background removal. No Ca was observed in the spectra recorded at a distance of 10 nm from the interface.

References

[1] D. B. Schwartz, P. M. Mankiewich, R. E. Howard, L. D. Jackel, B. L. Straughn, E. G. Burkhart, and A. H. Dayem, IEEE Trans. Magn. 25 (1989) 1298.

[2] M. S. Dilorio, S. Yoshizumi, K.-Y. Yang, and M. Maung, Appl. Phys. Lett. 58 (1991) 2552.

[3] N. Missert, T. E. Harvey, R. H. Ono, and C. D. Reintsema, Appl. Phys. Lett. 63 (1993) 1690.

[4] R. H. Ono, J. A. Beall, M. W. Cromar, T. E. Harvey, M. E. Johansson, C. D. Reintsema, and D. A. Rudman, Appl. Phys. Lett. 59 (1991) 1126.

[5] C. T. Rogers, A. Inam, M. S. Hedge, B. Dutta, X. D. Wu, and T. Venkatesan, Appl. Phys. Lett. 55 (1989) 2032.

[6] J. Gao, Y. Boguslavskij, B. B. G. Klopman, D. Terpstra, G. J. Gerritsma, and H. Rogalla, Appl. Phys. Lett. 59 (1991) 2754.

[7] J. Gao, W. A. M. Aarnink, G. J. Gerritsma, D. Veldhuis, and E. Rogalla, IEEE Trans. Magn. 27 (1991) 3062.

[8] J. B. Barner, C. T. Rogers, A. Inam, R. Ramesh, and S. Bersey, Appl. Phys. Lett. 59 (1991) 1629.

[9] E. Polturak, G. Koren, D. Cohen, E. Aharoni, and G. Deutscher, Phys. Rev. Lett. 67 (1991) 3038.

[10] B. D. Hunt, M. C. Foote, and L. J. Bajuk, Appl. Phys. Lett. 59 (1991) 982.

[11] D. K. Chin and T. Van Duzer, Appl. Phys. Lett. 58 (1991) 753.

[12] K. Char, M. S. Colclough, T. H. Geballe, and K. E. Myers, Appl. Phys. Lett. 62 (1993) 196.

[13] K. Char, L. Antognazza, and T. H. Geballe, Appl. Phys. Lett. 63 (1993) 2420.

[14] K. Char, Mat. Res. Bull. 19 (1994) 51.

[15] E. Olsson and K. Char, Appl. Phys. Lett. 64 (1994) 1292.

[16] S. Rozeveld, K. L. Merkle, and K. Char, J. Mat. Res., to be submitted (1994) .

[17] P. Stadelmann, Ultramicroscopy 21 (1987) 131.

[18] P. R. Van Loan, Ceramic Bull. 51 (1972) 231.

[19] J. D. Jorgensen, B. W. Veal, A. P. Paulikas, L. J. Nowicki, G. W. Crabtree, H. Claus, and W. K. Kwok, Phys. Rev. B 41 (1990) 1863.

[20] JCPDS, Powder Diffraction file: LaAlO3, Vol. 31-22 (Swarthmore, Pa., 1986), .

[21] JCPDS, Powder Diffraction file: CaRuO3, Vol. 25-172 (Swarthmore, Pa., 1986), .

[22] S. Geller and V. B. Bala, Acta. Cryst. 9 (1956) 1019.

[23] S. Geller, J. Chem. Phys. 24 (1956) 1236.

[24] J. B. Goodenough, Phys. Rev. 100 (1955) 564.

[25] P. C. Donohue, L. Katz, and R. Ward, Inorg. Chem. 4 (1965) 306.
[26] A. Callaghan, C. W. Moeller, and R. Ward, Inorg. Chem. 5 (1966) 1572.
[27] L. Katz and R. Ward, Inorg. Chem. 3 (1964) 205.
[28] S. J. Rozeveld, K. L. Merkle, and K. Char, unpublished research (1994) .
[29] N. Stenton, M. R. Notis, and D. B. Williams, J. Am. Cer. Soc. 67 (1984) 227.
[30] R. F. Egerton, Electron energy-loss spectroscopy in the electron microscopy, (New York, 1986), .
[31] S. Rozeveld, K. L. Merkle, and K. Char, in T. V. Duzer, Eds. *The 1994 Applied Superconductivity Conference*, Vol. submitted, IEEE Communications Society (1994) .

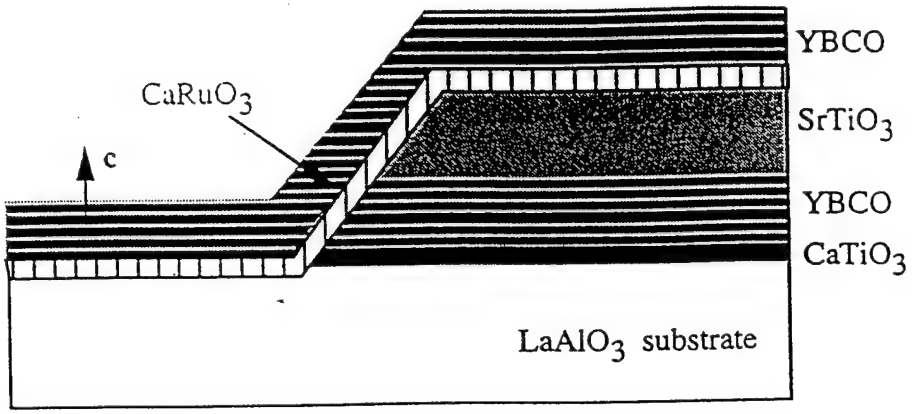

Fig. 1

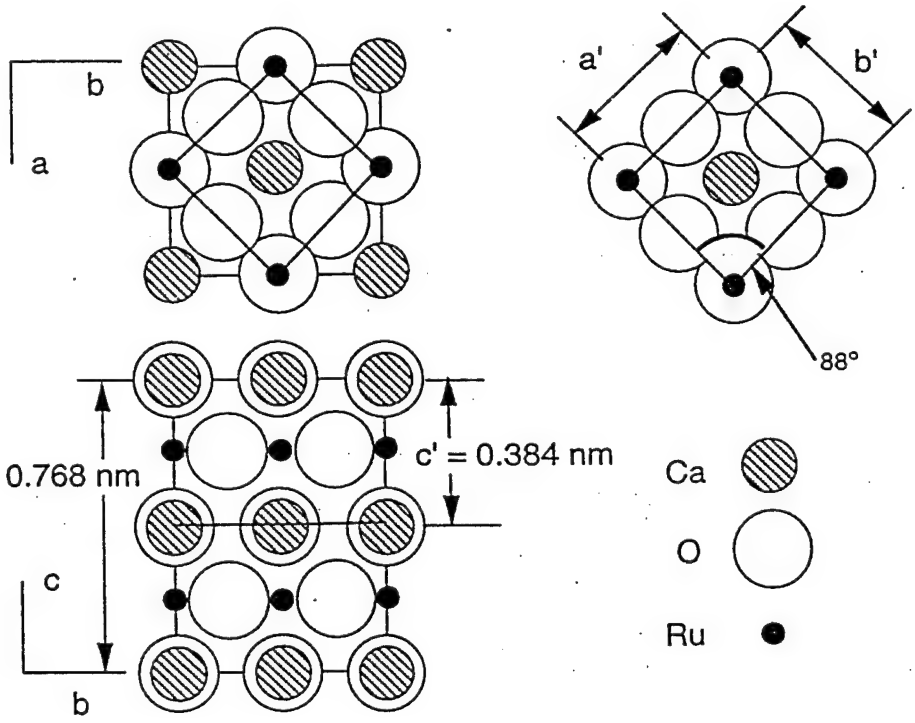

Fig. 2

$CaRuO_3$ Orthorhombic

a = 0.554 nm
b = 0.536 nm
c = 0.768 nm

Pseudo cubic cell

a' = b' = 0.385 nm
c' = 0.768 / 2 = 0.384 nm
$\alpha = \beta = 90^\circ$: $\gamma = 88^\circ$

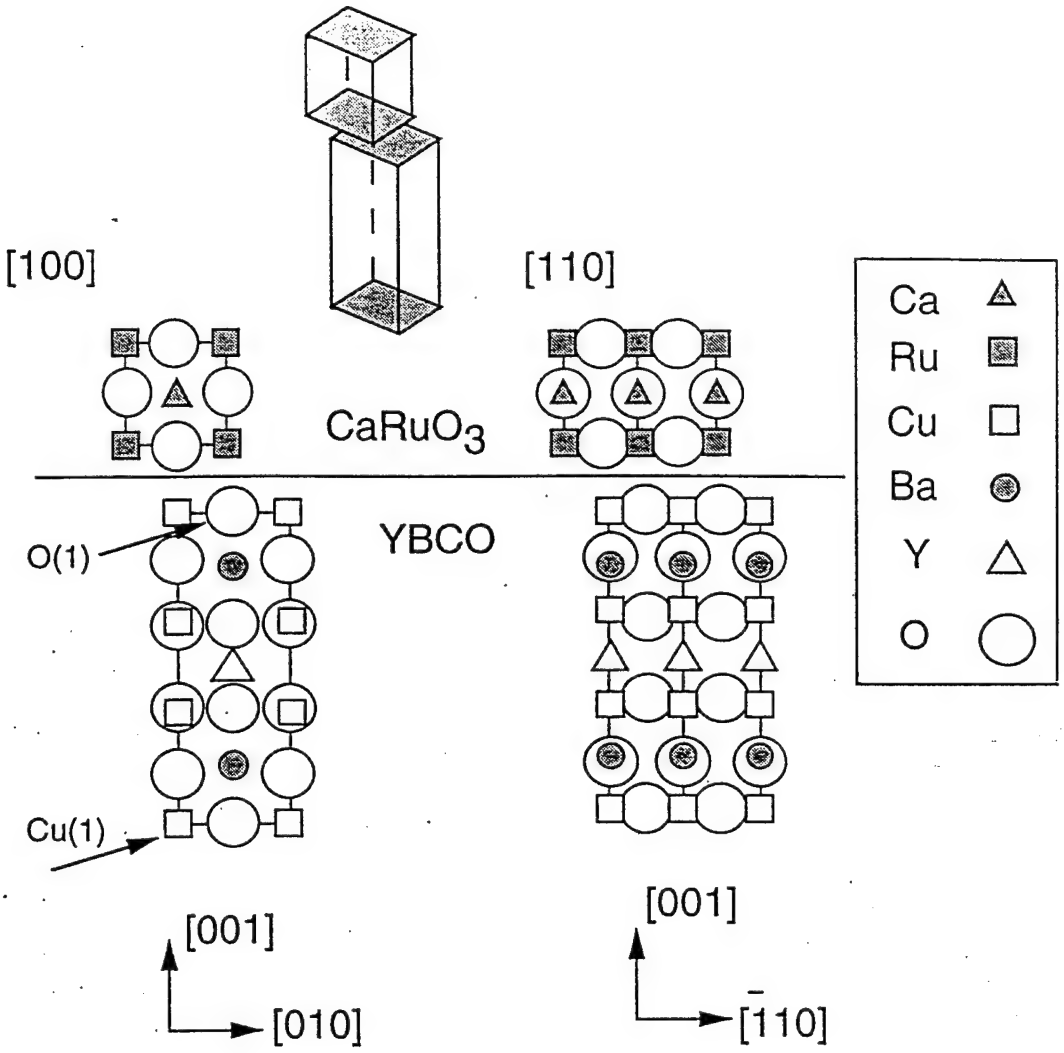

Fig. 3

YBCO
SrTiO3
YBCO
500 nm
LaAlO3

4

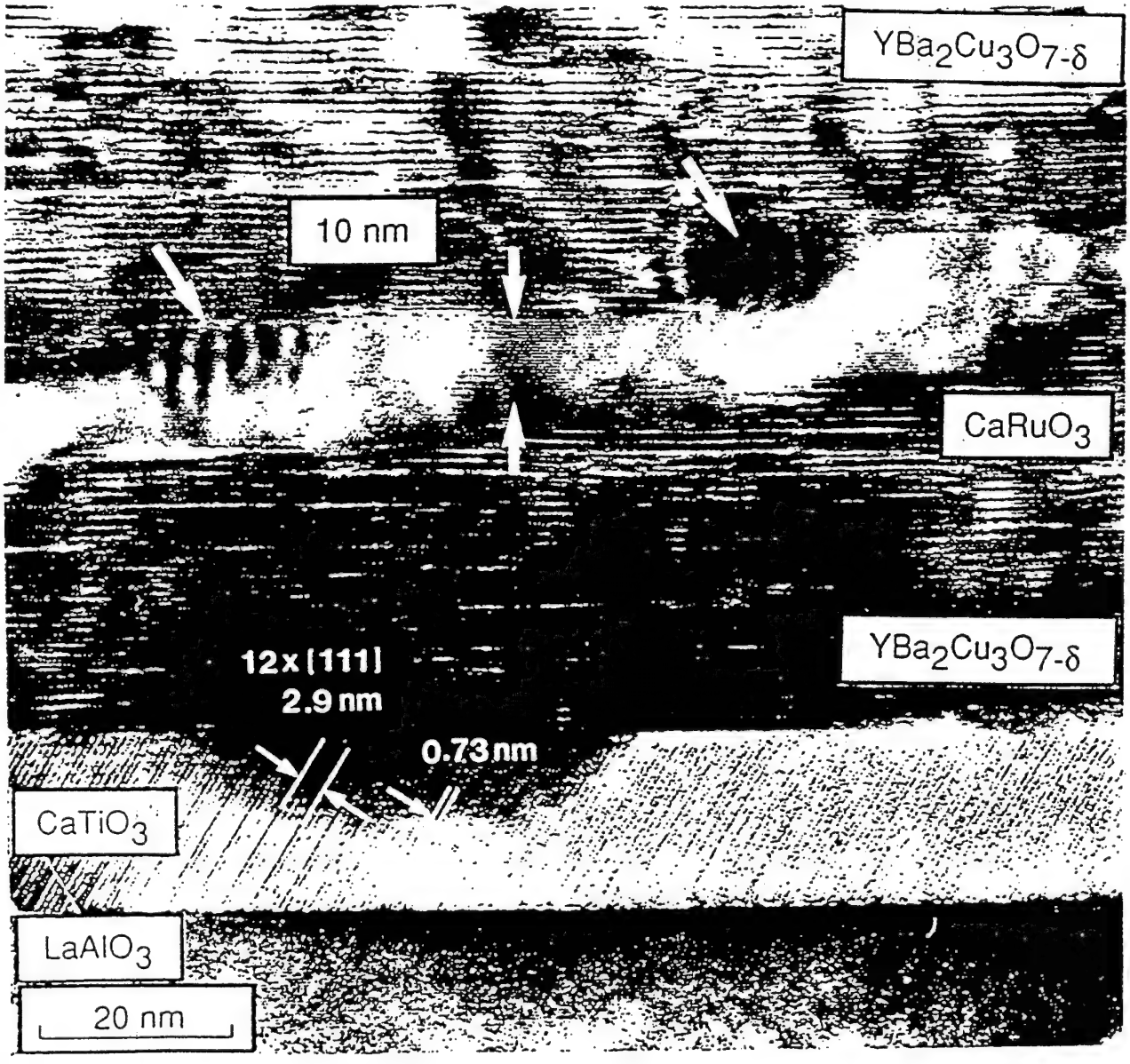
YBa2Cu3O7-δ
10 nm
CaRuO3
YBa2Cu3O7-δ
12x[111]
2.9 nm
0.73 nm
CaTiO3
LaAlO3
20 nm

5

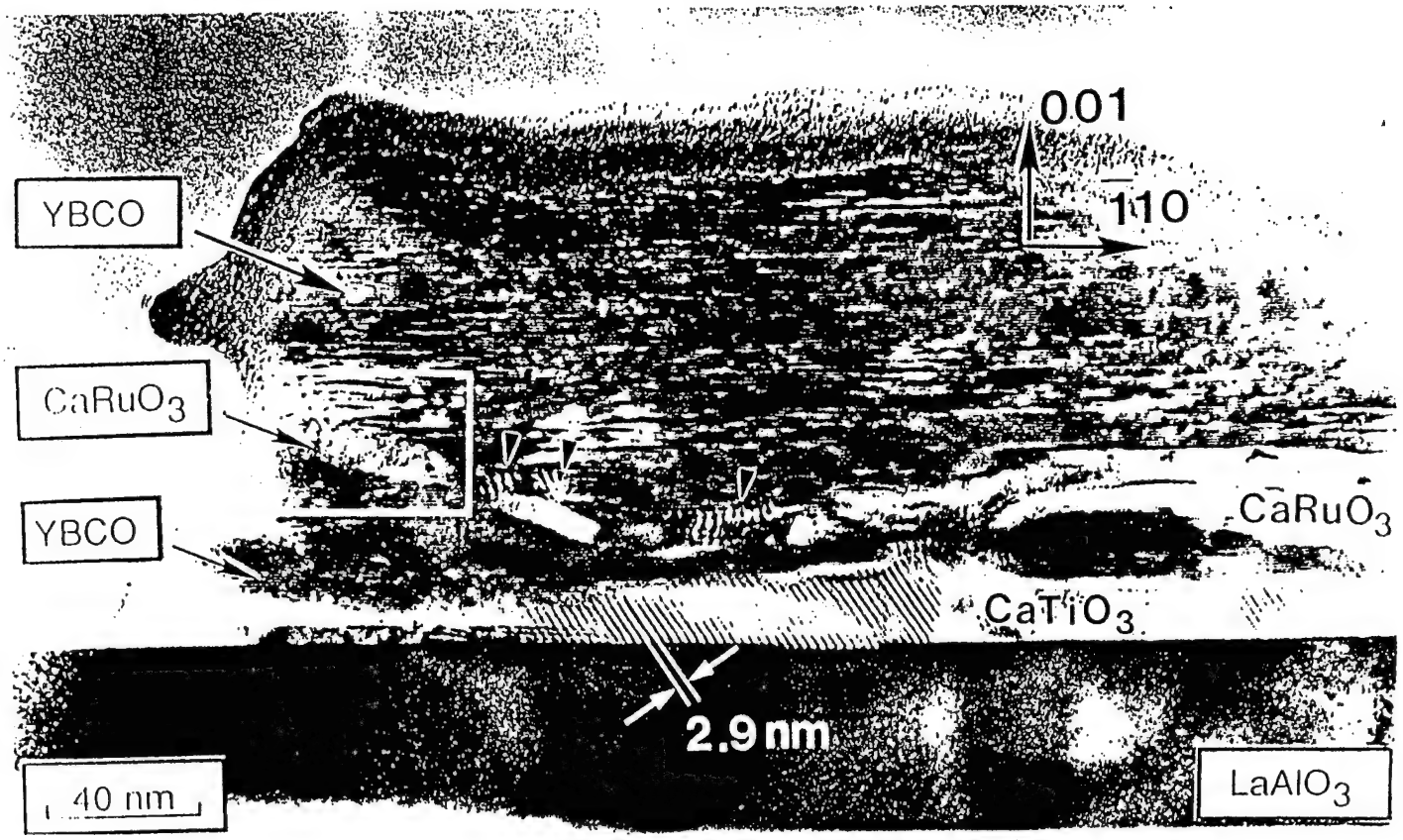

6

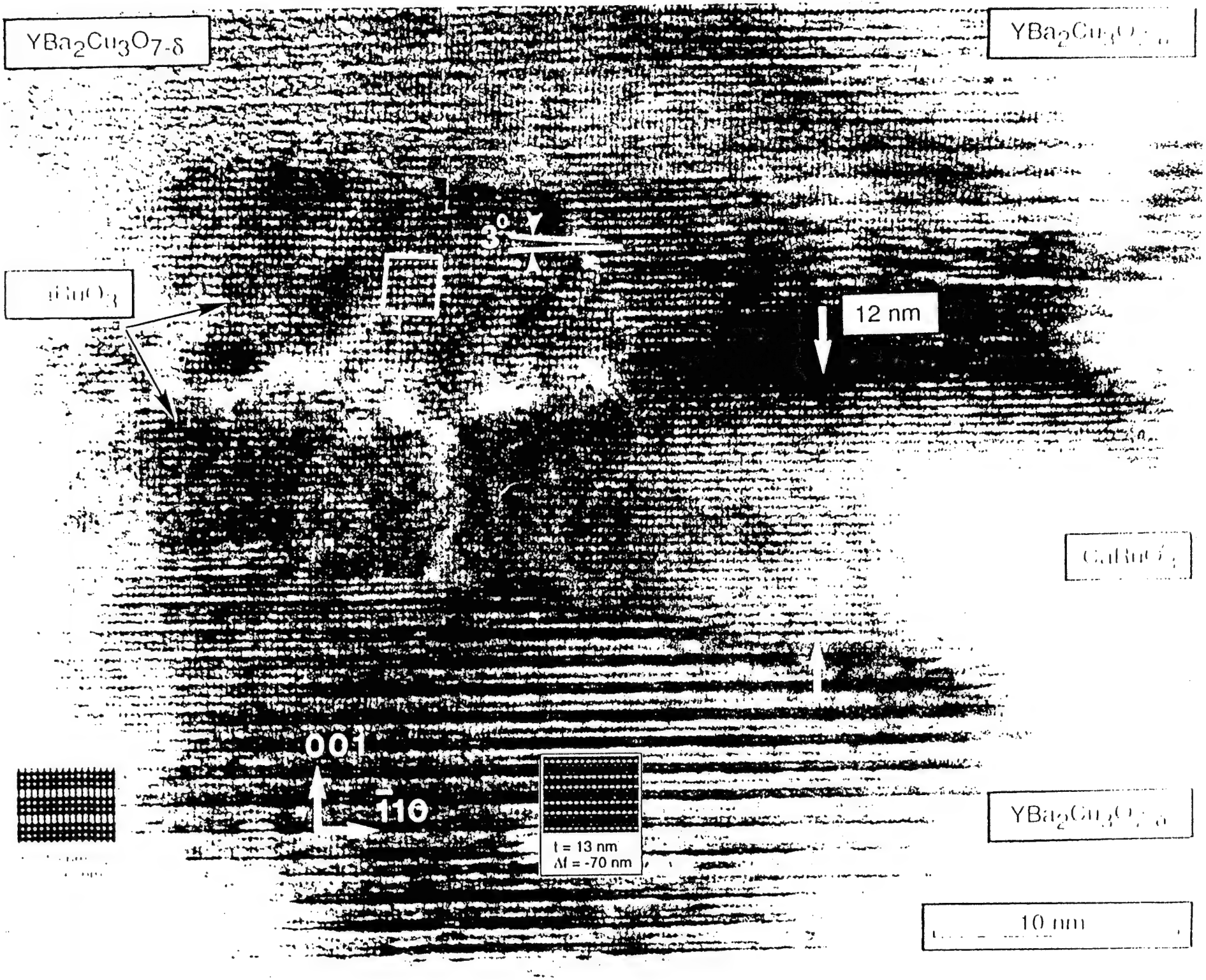
$YBa_2Cu_3O_{7-\delta}$
3°
12 nm
001
$\bar{1}10$
t = 13 nm
Δf = -70 nm
10 nm

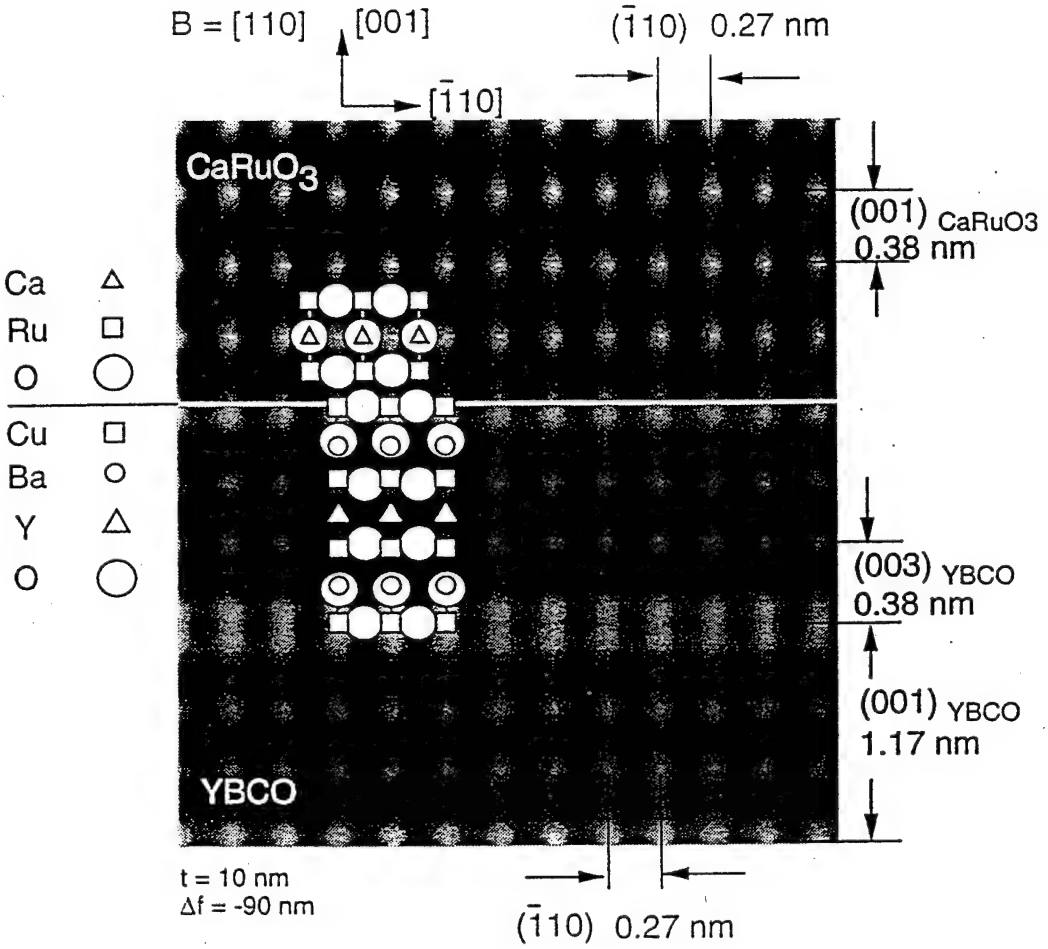
B = [110]
[001]
[$\bar{1}$10]
($\bar{1}$10) 0.27 nm
CaRuO3
(001) CaRuO3
0.38 nm
Ca
Ru
O
Cu
Ba
Y
O
(003) YBCO
0.38 nm
(001) YBCO
1.17 nm
YBCO
t = 10 nm
Δf = -90 nm
($\bar{1}$10) 0.27 nm

Fig. 8

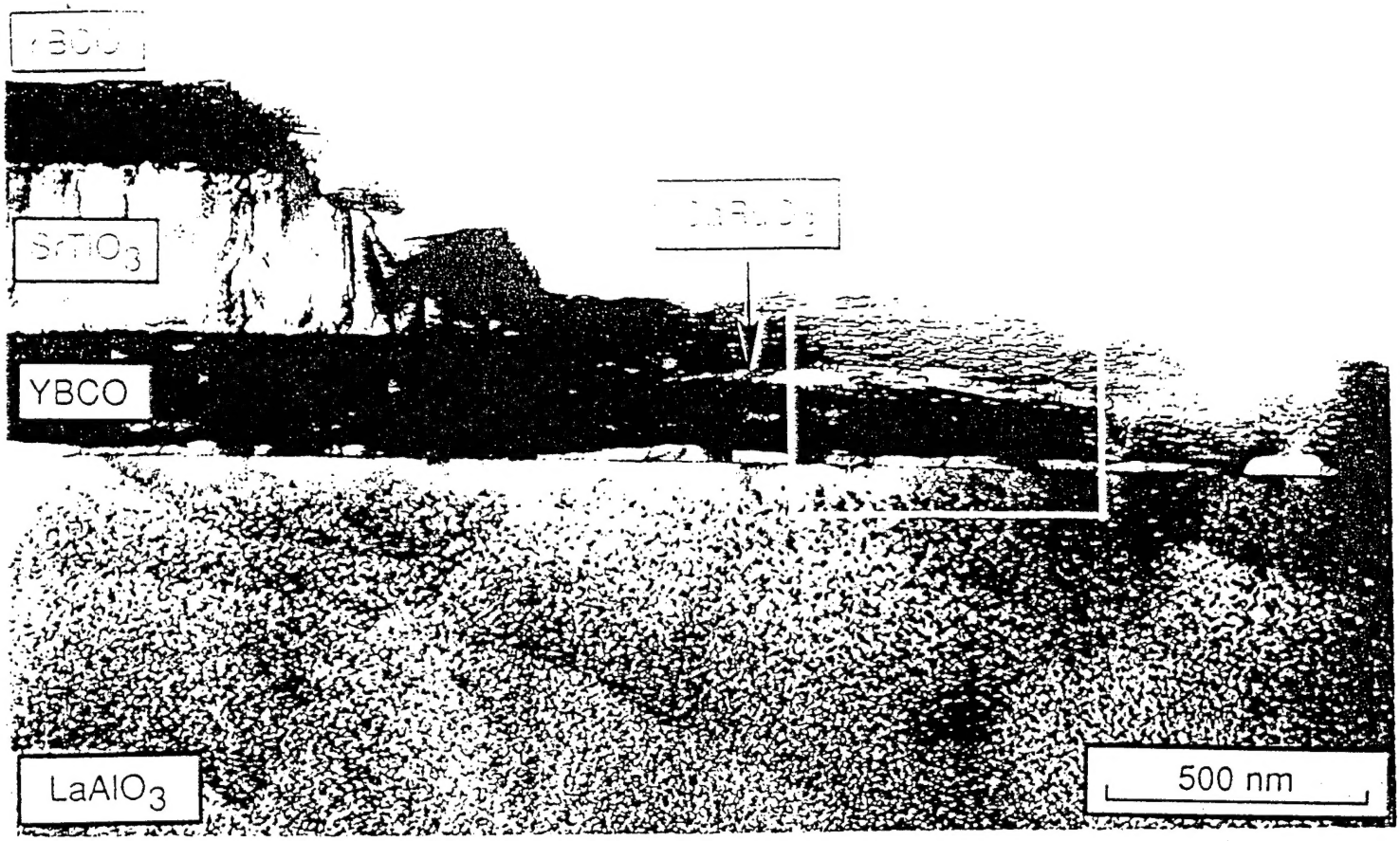
YBCO
$SrTiO_3$
YBCO
$LaAlO_3$
500 nm

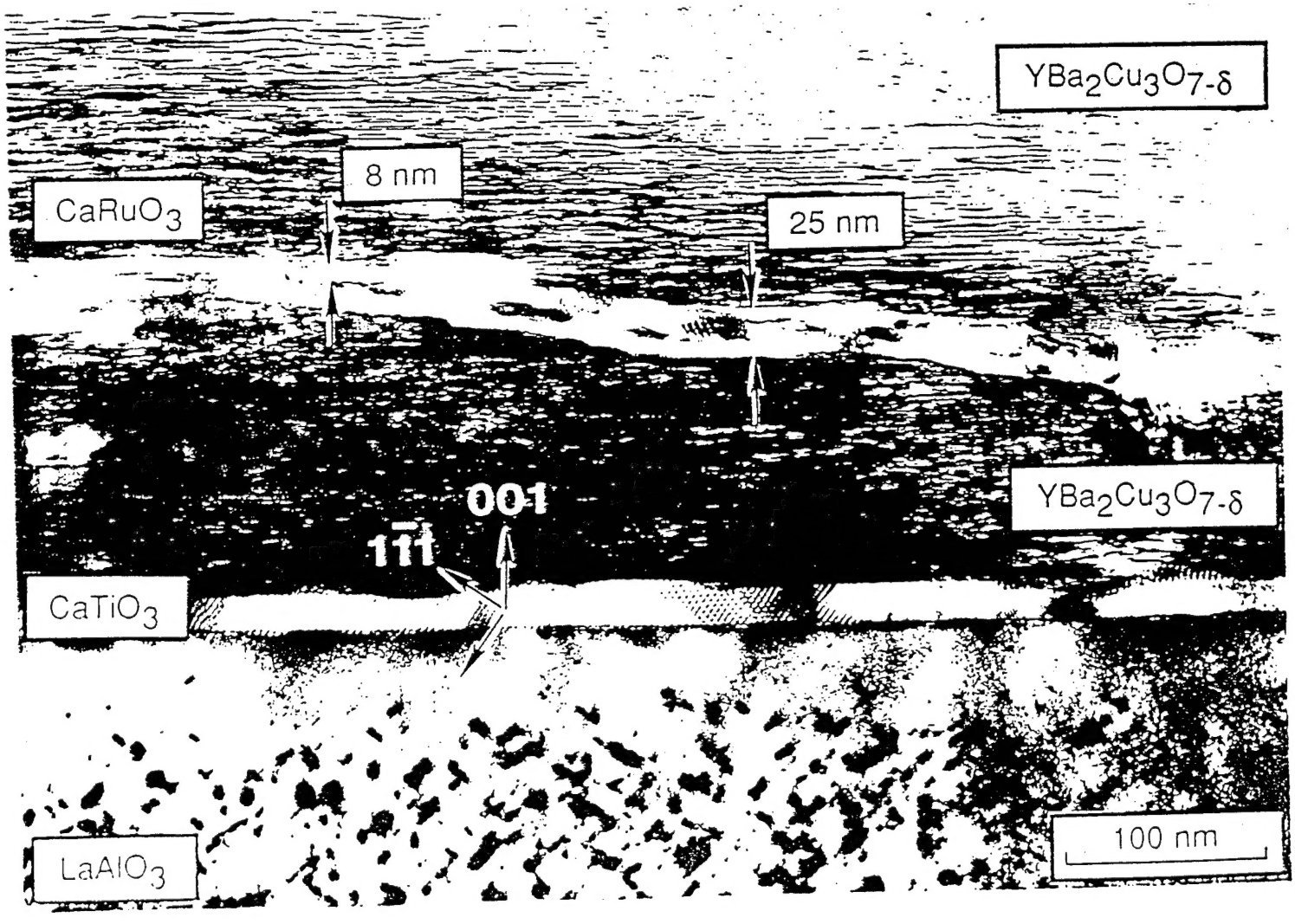
$YBa_2Cu_3O_{7-\delta}$
8 nm
$CaRuO_3$
25 nm
001
$\bar{1}11$
$YBa_2Cu_3O_{7-\delta}$
$CaTiO_3$
$LaAlO_3$
100 nm

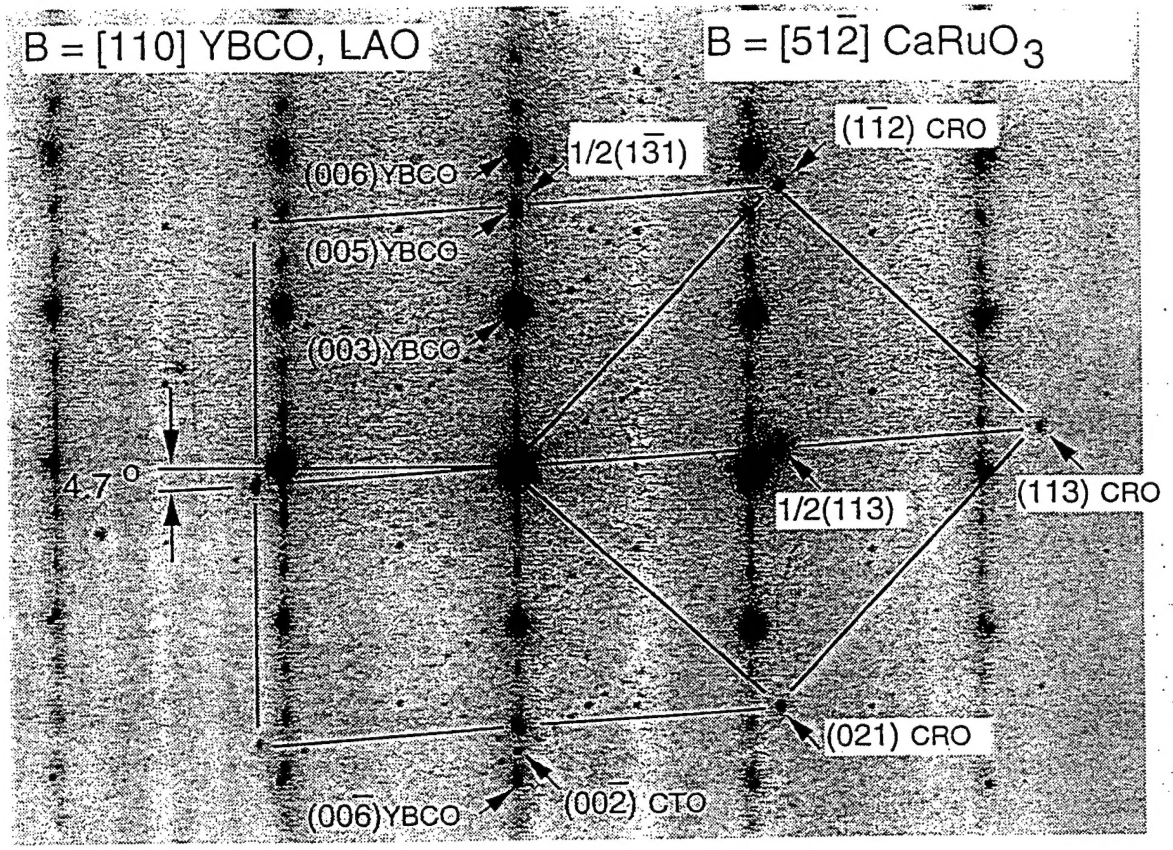
B = [110] YBCO, LAO
B = [5$\bar{1}\bar{2}$] $CaRuO_3$
(006)YBCO
1/2(1$\bar{3}$1)
(1$\bar{1}$2) CRO
(005)YBCO
(00$\bar{3}$)YBCO
4.7°
1/2(113)
(113) CRO
(021) CRO
(00$\bar{6}$)YBCO
(00$\bar{2}$) CTO

Fig

11

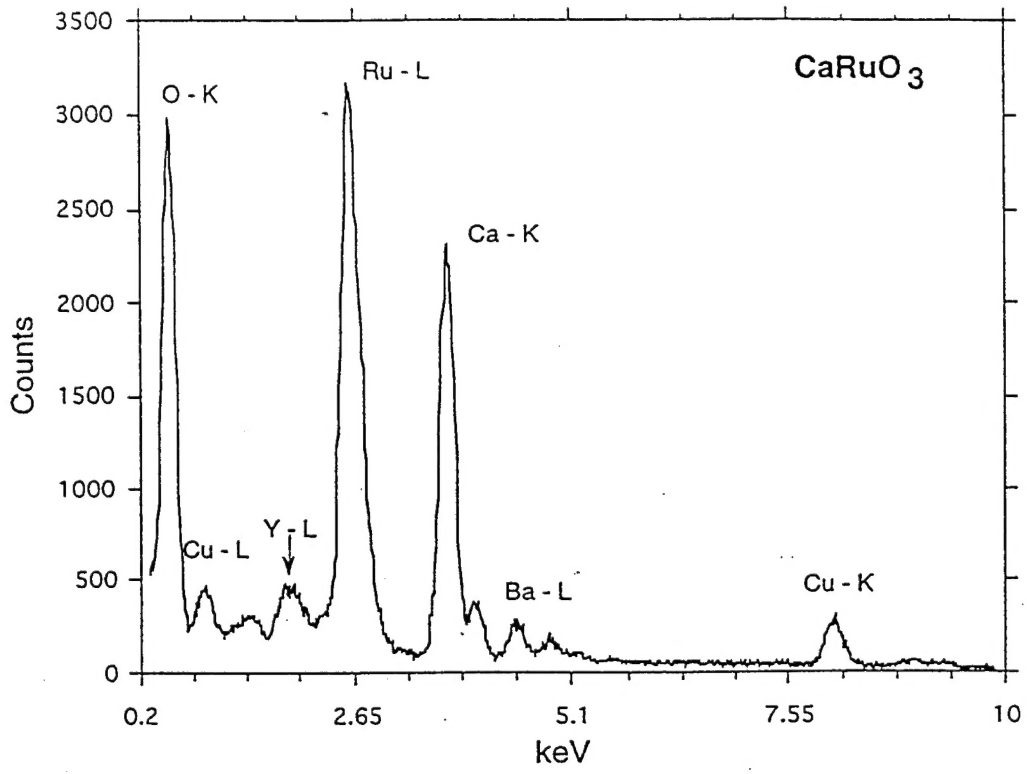
3500
3000
2500
2000
1500
1000
500
0
Counts
O - K
Ru - L
CaRuO 3
Ca - K
Cu - L
Y - L
Ba - L
Cu - K
0.2
2.65
5.1
7.55
10
keV

Fig. 12

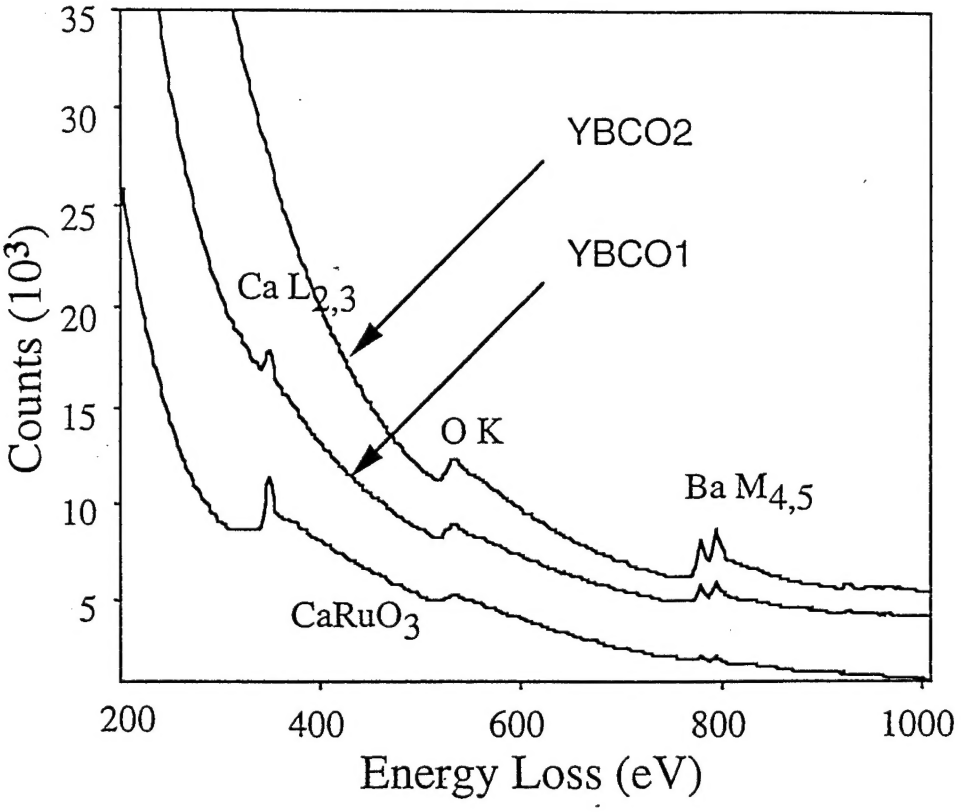

Fig. 13a

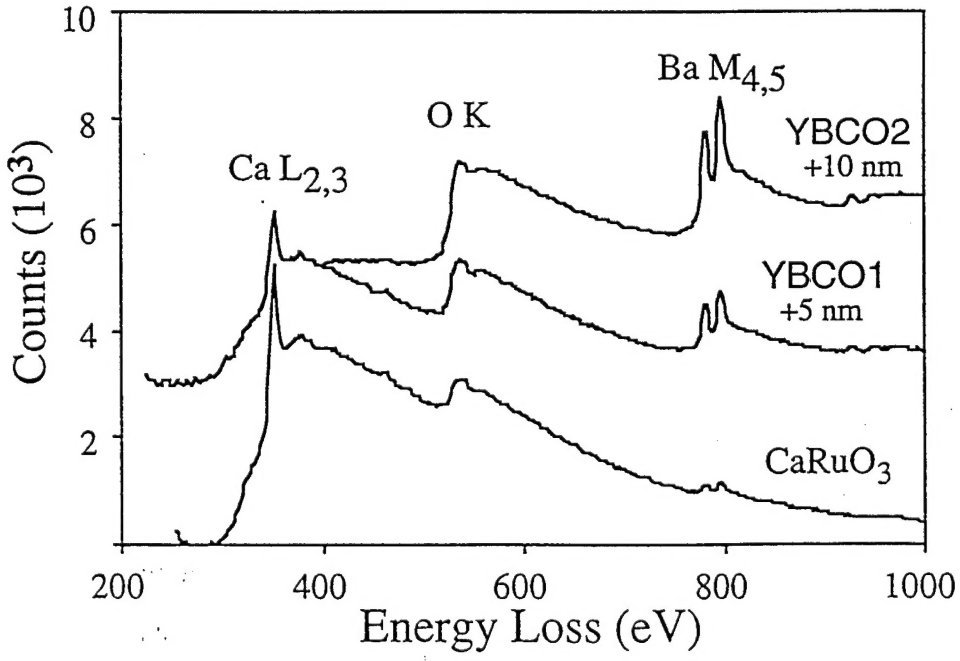

Fig. 13b